Exploring the influence of porosity and thickness on lithium-ion battery electrodes using an image-based model

Adam M. Boyce[a,b], *Xuekun Lu*[a,b], *Dan J. L. Brett*[a,b] *and Paul R. Shearing*[a,b]*

[a]Electrochemical Innovation Lab, Department of Chemical Engineering, University College London, London WC1E 7JE, UK

[b]The Faraday Institution, Quad One, Becquerel Ave, Harwell Campus, Didcot, OX11 0RA, UK

*Corresponding author e-mail: p.shearing@ucl.ac.uk

Abstract

There is a growing need for lithium-ion batteries that possess increased energy storage capabilities, with a simultaneous requirement for fast charging and improved rate performance. Thick electrodes provide proportionately more active material and thus better storage capabilities, while having the unavoidable characteristic of an increased diffusion length that adversely affects the high rate performance of an electrode. Here, the workflow of advanced X-ray nano-computed tomography (CT) imaging, morphological image processing techniques, and a coupled electrochemical model is established. This tool facilitates the digital alteration of realistic electrode microstructures in a rational manner and permits studies such as the one presented in this work where an extensive parametric study is carried out and assesses the influence of thickness, porosity and discharge rate on electrode performance under the theme of heterogeneity, a key advantage of image-based analysis. In broad terms, the model shows significant heterogeneities in lithium, lithium-ion, and current density distributions across the electrode that give rise to the significant and inextricable link between thickness, porosity and discharge rate. The modelling methodology presented in this work provides a foundation for the design of novel thick battery electrodes, and an example of such a design is presented here.

Keywords: lithium-ion battery, image-based model, porosity, thick electrode, microstructure

1. Introduction

Design and optimisation of a lithium-ion battery (LIB) microstructure is a crucial element in the search for energy storage solutions with increased capacity and improved high-rate capabilities. This is of significant interest to myriad industries, one of which is the automotive sector, where fast charging of electric vehicles and improvement of range are of utmost concern in order to increase uptake in use, a key strategy in the reduction of global CO_2 emissions. One particular area of interest for increased energy storage is the optimisation of electrode thickness where it may be possible for significant gains in capacity. A lithium-ion battery electrode is a highly heterogeneous composite with a microstructure that typically comprises active material where lithium is stored, a porous domain filled with electrolyte where lithium ions are transported, and a conductive additive (carbon binder domain-CBD) which permits electron conduction. The electrodes are usually ~80 μm or less in thickness with a high proportion of inactive material or CBD. If thicker electrodes are used then significant (>30%) increases in material loading can be achieved, see Kuang et al. [1] and discussion in Boyce et al. [2].

However, there are significant barriers that prevent the use of thick electrodes in conventional electrodes. Once the thickness of an electrode is increased, transport related limitations become important [3,4]; the required diffusion length for lithium ion transport extends, resulting in the possibility of reduced utilisation of storage materials at the extremities of the electrode, adjacent to the current collector. The CBD is a nanoporous foam-like structure that is distributed in a heterogeneous manner throughout the electrode. This multiscale structure presents a tortuous path that can drastically increase the diffusive length scale [5] and becomes even more pronounced when the electrode is thicker. In addition, thick electrodes are difficult to manufacture, and challenges exist on numerous fronts; it is difficult to dry them in a homogenous manner or without severe, detrimental cracking, while it is also challenging to maintain calendering process quality [2].

There have been a wide variety of efforts made to alter the pore microstructure of electrodes to facilitate improved transport behaviour [6–11]. For example, in an effort to reduce the tortuous pathways for thick electrodes, Huang et al. [12] and Elango et al. [13] used directional templating to provide channels for improved ionic transport in graphite and $LiFePO_4$ electrodes respectively, whilst Huang and Grant [14] attempted a similar methodology with coral-like patterns in LCO cathodes. Billaud et al. [15] used a magnetic alignment approach to orientate graphite particles; this yielded a threefold increase in the capacity of thick graphite electrodes (~200μm). Sander et al. [16] used a similar approach for aligning particles within a $LiCoO_2$ electrode.

Modelling of batteries typically occurs at three different length scales, comprising the single particle, electrode microstructure, or the cell level. Theoretical and numerical modelling of such electrochemical systems may be achieved by the quasi-2D Doyle-Fuller-Newman (DFN) model developed by Doyle et al. [17]. Typically, such modelling involves significant levels of homogenisation of the underlying highly heterogeneous microstructure due to computational expense or the desire to optimise battery performance rapidly. The reader is pointed to the following articles for a comprehensive review on continuum electrochemical modelling [18,19], however, related to the present work, we note the following studies: Park et al. [20] produced a semi-empirical model in which they predicted the drop off in capacity when thick electrodes are discharged, particularly at higher rates; Suthar et al. [21] explored the influence of porosity, thickness, and discharge rate of graphite electrodes using a pseudo 2D (P2D) model, highlighting reduction in discharge capacity for thicker electrodes with lower porosity; Xu et al. [22] performed similar, but wider ranging thickness-based analysis using a homogenised physics based approach with idealised 2D geometry to show that significant under-utilisation of active materials occurs at moderate electrode thicknesses (~130 μm) whilst showing a reduction in rate performance; Finally Heubner et al. [23] produced a simplified and

homogenised theoretical model highlighting the relationship between porosity, thickness and discharge rate. However, 2D investigations are limited in scope due to the simplification of the complex 3D microstructure (and thus the heterogeneities), which are known to play a significant role in determining the rate performance, a topic we address in the present work.

Image-based modelling has emerged as a powerful technique for understanding the microstructural behaviour of lithium-ion battery electrodes [24–31]. The technique involves the creation of a computational mesh that is based on imaging techniques such as X-ray CT. The mesh then forms the basis for a highly coupled, multiphysics simulation, and for lithium-ion batteries this usually comprises electrochemistry and diffusive transport, as well as thermal and mechanical behaviour in some cases [32]. The advantage of image-based modelling is that the microstructure is typically fully resolved with minimal homogenisation of the underlying physical equations. Hence, it is possible to capture a wide range of heterogeneities in microstructure morphology and the resulting influence on electrode performance, e.g. particle shape, carbon binder distributions, amongst others, see Muller et al. [33] for example. Recent studies, such as those by Lu et al. [34,35] and Ferraro et al. [36] have highlighted how these methods can be used to aid in the design of improved lithium-ion battery electrodes. For example, Lu et al. [34] showed that designing electrodes with gradients in particle size results in improved energy storage capabilities. Furthermore, Kremer et al. [27] explored the influence of drying temperature during thick electrode manufacture and used image-based models to compare against experiment. Danner et al. [29] used binary image-based models (particle and pore) with artificially introduced carbon binder to assess the difference in a 70 µm and 320 µm electrode and showed that the thicker electrode had reduced specific energy storage capabilities due to reduced porosity. Image-based models have not, however, been used to explore the relationship between electrode porosity and thickness in a comprehensive manner. The use of image processing techniques such as morphological operations and an image-based model

framework for this purpose also permits detailed insight into the local heterogeneities that occur within a LIB.

Here, we present a systematic and comprehensive parametric study in which we computationally alter the porosity of a 3D X-ray CT, image-based electrode microstructure using morphological operations, while simultaneously altering the electrode thickness via image mirroring. The resulting microstructures form the basis for a coupled physics-based electrochemical and species transport model. The model allows us to establish a relationship between rate, porosity, and thickness, while also providing a deeper insight into the underlying microstructural behaviour when these parameters are adjusted. We present a platform which facilitates a deeper understanding of thick electrode behaviour and provides a tool enabling the design of next generation electrodes with higher capacity and improved transport characteristics.

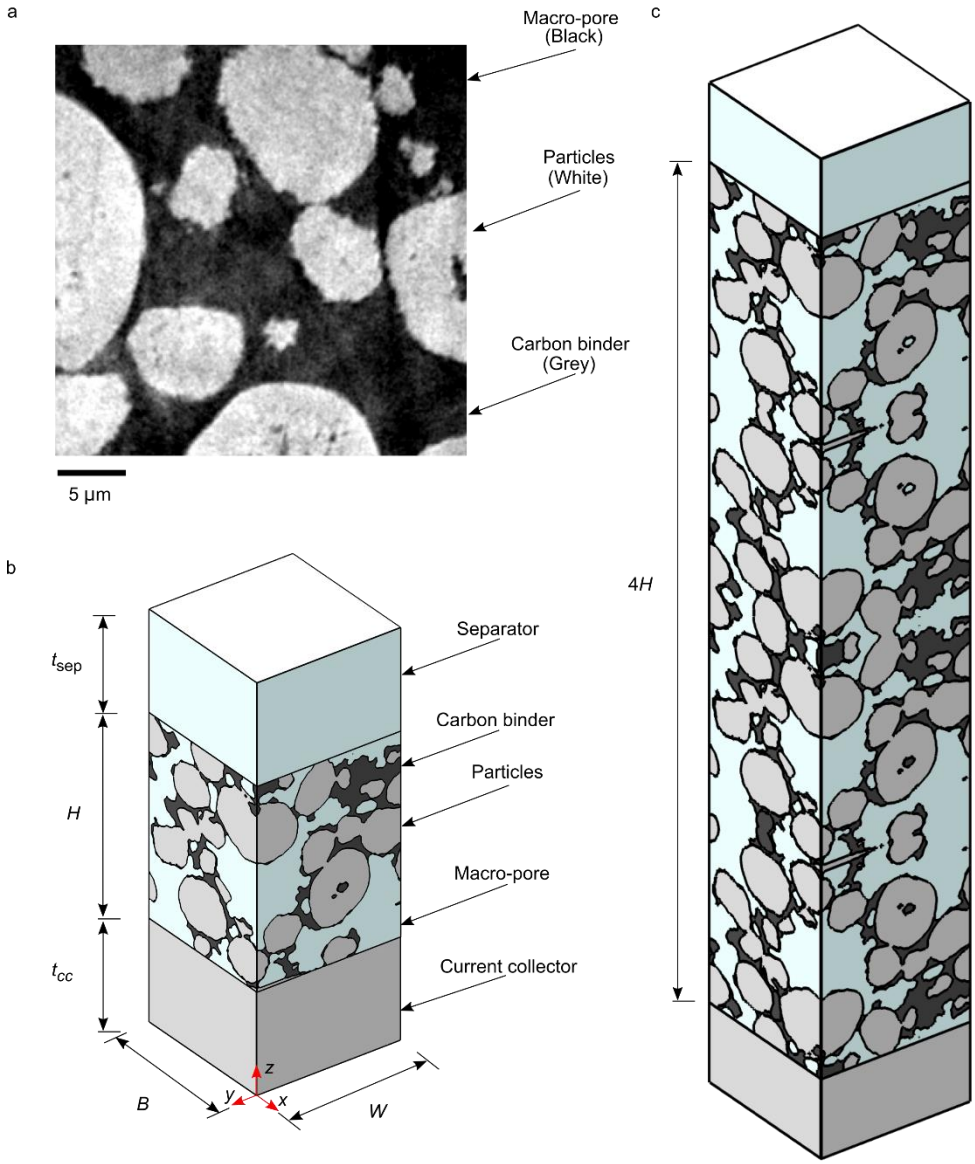

Fig. 1. (a) A sample slice from an X-ray nano-CT scan with particles (white), CBD (grey) and pores (black). (b) Segmented and model geometry of the base sample where H=40 µm. (c) An example of a computationally mirrored sample where the electrode thickness is 160 µm. The macro-porosity is 20% in (b) and (c), and B=W=30 µm, and t_{cc}= t_{sep}=15 µm in all cases.

2. Experimental and numerical methods

2.1 Materials

A calendered $LiNi_{0.6}Mn_{0.2}Co_{0.2}O_2$ (NMC 622) cathode (AGM Batteries Ltd, UK) with a mass loading of 130 g m^{-2} was used in this study. The weight ratio of the constituents is 94.5:3:2.5 for the active material (BASF, Germany), conductive carbon (C65, KS6L 2:1) and binder (PVDF, Solref), respectively.

2.2 Image acquisition

The sample to be scanned was cut into a 1 mm disk from the electrode sheet and glued onto the tip of a pin using an epoxy adhesive. The diameter was further reduced to approx. 75 μm by laser milling to ensure sufficient X-ray transmission and signal-to-noise ratio [37]. A Zeiss Xradia Ultra 810 X-ray macroscope [38] (Carl Zeiss, CA, USA) with a quasi-monochromatic parallel beam (5.4 keV) was used to collect 1201 radiographic projections (exposure time 60 seconds/frame) at the voxel size of 126 nm over the sample rotation of 180º. A standard filtered back-projection algorithm [39] was used to reconstruct the 3D volume of the electrode from the acquired projections.

2.3 Image processing

The raw CT image was processed using Avizo software (Avizo, Thermo Fisher Scientific, Waltham, Massachusetts, U.S.). A non-local means filter was applied to the carbon binder phase to provide a smoother domain for meshing. A volume of interest with initial electrode thickness of 40 μm and a cross section of 30 μm x 30 μm was considered. Note that the carbon binder phase contains internal nano-porosity that is difficult to resolve and is thus accounted for by using an effective medium approximation, hence the smoothing has no influence on simulation results. A virtual slice from the 3D tomogram of the processed image can be seen in Fig. 1a. The watershed algorithm was used to segment the raw image into three phases (i.e.

macro-pore, CBD, and particles) using Avizo. The segmentation process yielded a ternary electrode image with the following volume fractions: 52.8% Particle, 34.4% macro-pore, and 12.8% carbon binder.

Morphological operations were used to manipulate the macro-porosity of the as-prepared microstructures. This was carried out using Simpleware ScaniP (Mountain View, California, U.S). A series of erosion and dilation operations were performed in which an erosion operation removed a given number of voxels from a target phase, while conversely, a dilation operation expanded the phase. The overall shape of the manipulated region is usually dictated by the structuring element and in this case a spherical element was used. In essence, the operations manipulate the voxels of a given phase by shrinking the phase at the boundary with the adjacent phases. The macro-porosity was altered by manipulating the carbon binder phase and the macro-pore phase only; for example, to reduce the porosity, the pore phase was removed using an erosion operation and then the empty voxels were replaced with CBD phase. The active material particles were not manipulated and a constant mass loading was maintained across the entire study. A detailed description of morphological operations and algorithms may be found here [40,41].

2.4 Finite element implementation

Simpleware ScaniP was used to mesh the segmented images, giving approximately 3.6-21 million linear tetrahedral elements, with 11.6-20 million degrees of freedom, depending on electrode thickness. The model framework and parameters, as outlined in Boyce et al. [32], were implemented in the finite element software COMSOL Multiphysics (v5.6, Sweden) using a 3D tomography-based mesh. We include a summary of the model framework and material parameters in Supplementary Information. Note that we neglect any mechanical and phase field terms, which were described in [32]. The Parallel Direct Sparse Solver (PARDISO) was used

to solve the discretised transport and electrode kinetics equations. A segregated approach was taken which involved solving the coupled field variables in a sequential, staggered way [42]. Time stepping was handled using 2nd order backward Euler differentiation.

2.5 Simulation details

A parametric study was carried out in which the thickness, porosity, and discharge rate of an image-based electrode model were all varied. A 40 µm electrode was chosen as the base thickness (see Fig. 1b), and then computational mirroring was used to replicate the microstructure to thicknesses of 80 µm, 160 µm, and 320 µm (see Fig. 1c). The 40 µm electrode was chosen to be representative of a typical commercial electrode. The thicknesses thereafter were chosen to assist in understanding the relationship between thickness, porosity and discharge rate, and exploring the microstructural design space. The as-manufactured macro-porosity was 35% and this served as the base specimen. The macro-porosity was subsequently altered to 20%, 25%, 30% and 40% using morphological operations, as described previously. All electrodes, with the exception of the 320 µm image, were discharged at 0.1C, 1C, 2.5C, and 5C. Due to significant computational expense, the 320 µm electrode was discharged at 1C and 5C only for a single macro-porosity of 25%.

3. Results and discussion

In broad terms, the electrochemical performance has been found to be strongly affected by electrode thickness, porosity, and discharge rate. This is illustrated in Fig. 2a and b, which shows the half-cell voltage versus capacity response due to change in macro-porosity and thickness. There is a clear increase in 1C discharge capacity when the porosity of a thick electrode is increased (Fig. 2a), whilst we observe a severe reduction in capacity when the thickness of an electrode is increased from 40 µm to 320 µm (Fig. 2b). Furthermore Fig. 2c summarises the results of the parametric study, illustrating the complex relationship between

electrode thickness, porosity and discharge rate, a matter which will be discussed in more detail in the ensuing sections. In addition, we have carried out electrochemical testing of the 40 μm, 35% macro-porosity base electrode and compared with the simulated response; further details can be found in the SI.

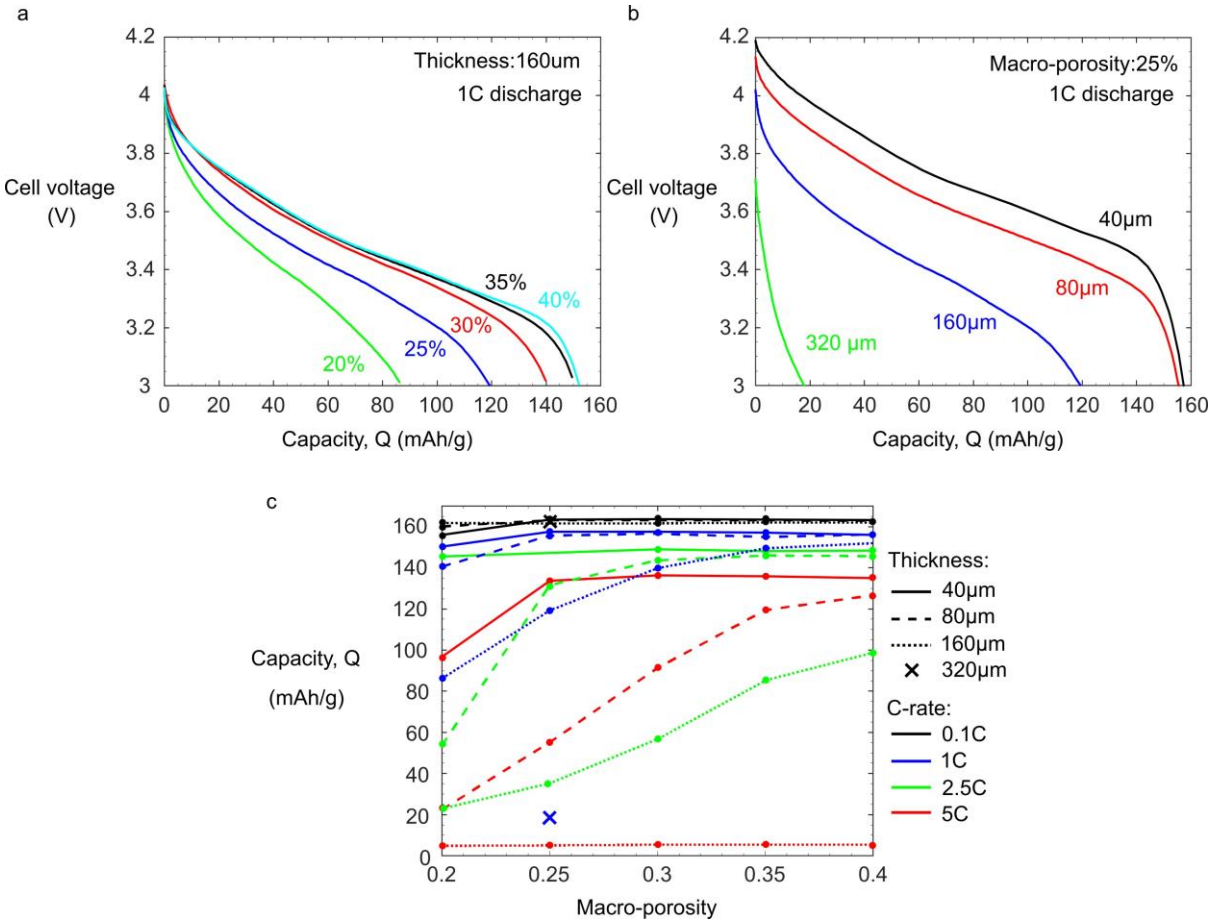

Fig. 2. (a) Discharge response of an electrode with varying macro-porosity, a fixed thickness of 160 μm and discharge rate of 1C. (b) Discharge response of an electrode with varying thickness, fixed macro-porosity of 25% and discharge rate of 1C. (c) Specific capacity as a function of macro-porosity for a variety of electrode thicknesses and discharge rates.

3.1 Electrode thickness considerations

Once the thickness of the electrode is increased we observe severe reductions in discharge capacity, see Fig. 2c, which can be attributed to the associated increase in diffusion length. In addition, this is further exacerbated by the tortuous path that the lithium ions take through the macrostructure during discharge. We may interpret this behaviour through the state of lithiation, lithium ion distributions, and charge transfer current profiles for electrodes of

varying thickness at discharge rates of 5C, as shown in Fig. 3. We observe particle-level gradients in lithium concentration irrespective of the electrode thickness, which is attributed to the slow diffusion of lithium in NMC particles, where the steepest gradients occur in larger particles. At the electrode-level we show that the highest concentration levels exist in the near-separator region which is to be expected given that the highest lithium-ion concentrations exist here. Subsequently, at points further into the electrode, we see lower states of lithiation and in general we observe steep gradients in lithium concentration. If the electrode thickness is increased then so is the diffusion length, and this is confirmed in our model by the increasing severity in concentration gradients across the electrode.

These trends are quantified in further detail in Fig. 4a where we observe significant heterogeneity in the state of lithiation at the centre of the particles across the electrode for a 40 μm and 80 μm electrode at 100% degree of discharge (5C discharge, 25% macro-porosity). In Fig. 4b, the electrolyte concentration is measured in 10 × 10 grids of equally-spaced discrete points at slices throughout the thickness of the same 40 μm and 80 μm electrodes. Note that some of the points overlap with particles and were thus excluded from analysis. We show that there is a very low presence of lithium ions in the regions near the current collector and throughout much of the electrode in general, which explains the poor lithiation characteristics. A high level of lithium-ion concentration is observed in the separator region that builds up due to the rapid discharge rate (5C), i.e. lithium-ion flux, and thereafter a steep gradient and drop off in concentration at a normalised distance of 0.6-0.8 from the current collector. This gradient can be attributed to sluggish diffusion in the electrolyte and demonstrates the limiting effect of utilising a thicker electrode microstructure. Another significant highlight here is the wide variation in electrolyte concentration across a single slice of cross-section. For example, if we take a slice at the fractional distance of 0.8 from the current collector for an 80 μm electrode in Fig. 4b, we can see that the maximum electrolyte concentration is 4.7 times that of the

minimum concentration. For the 40 µm electrode this factor reduces to 1.6. Multiple conclusions can be drawn here: first, significant heterogeneity exists within the electrode, which we attribute to the complex tortuous microstructure; second, this will naturally lead to heterogeneity in the exchange current density and thus electrochemical reactions (see Fig. 3), resulting in uneven lithiation. In addition, the variation in particle size will lead to further heterogeneity; small particles will lithiate much faster and in a more uniform manner than larger particles, as described previously, giving lower surface concentrations. In summary, it is clear that the degree of microstructure-induced heterogeneity in electrolyte concentration is inextricably linked with other factors such as the electrode thickness and thus the ability to diffuse into the remainder of the microstructure.

If we now consider the exchange current density in more detail (Fig 3.), then we can see that higher levels of current density are present in narrow bands within thicker electrodes. This implies that charge transfer reactions are occurring at very high rates in a very heterogeneous fashion giving larger cell resistance and under-utilisation of active material. This is confirmed by the trends of Fig. 2c. In contrast, the thin electrodes possess a reasonably homogenous and generally lower current density within the electrode, indicating improved active material utilisation and hence a higher capacity.

Furthermore, we can see that the most severe reduction in capacity occurs as thicker electrodes, e.g, 80 µm, 160 µm and by extension 320 µm (not shown), are discharged at high rates, see the corresponding curves for the 2.5C and 5C discharges in Fig. 2c. There exists a balance between the reaction kinetics, solid-state diffusion within the particles, and the transport of charge carriers within the electrolyte. When the charge transfer reactions at the particle-electrolyte interface are occurring at a high rate (as is the case for a 5C discharge), then there is insufficient time for the lithium ions to diffuse into the depths of the electrode, away from the separator.

This results in a significant increase in overall cell resistance and under-utilisation of the active materials, resulting in lower capacity.

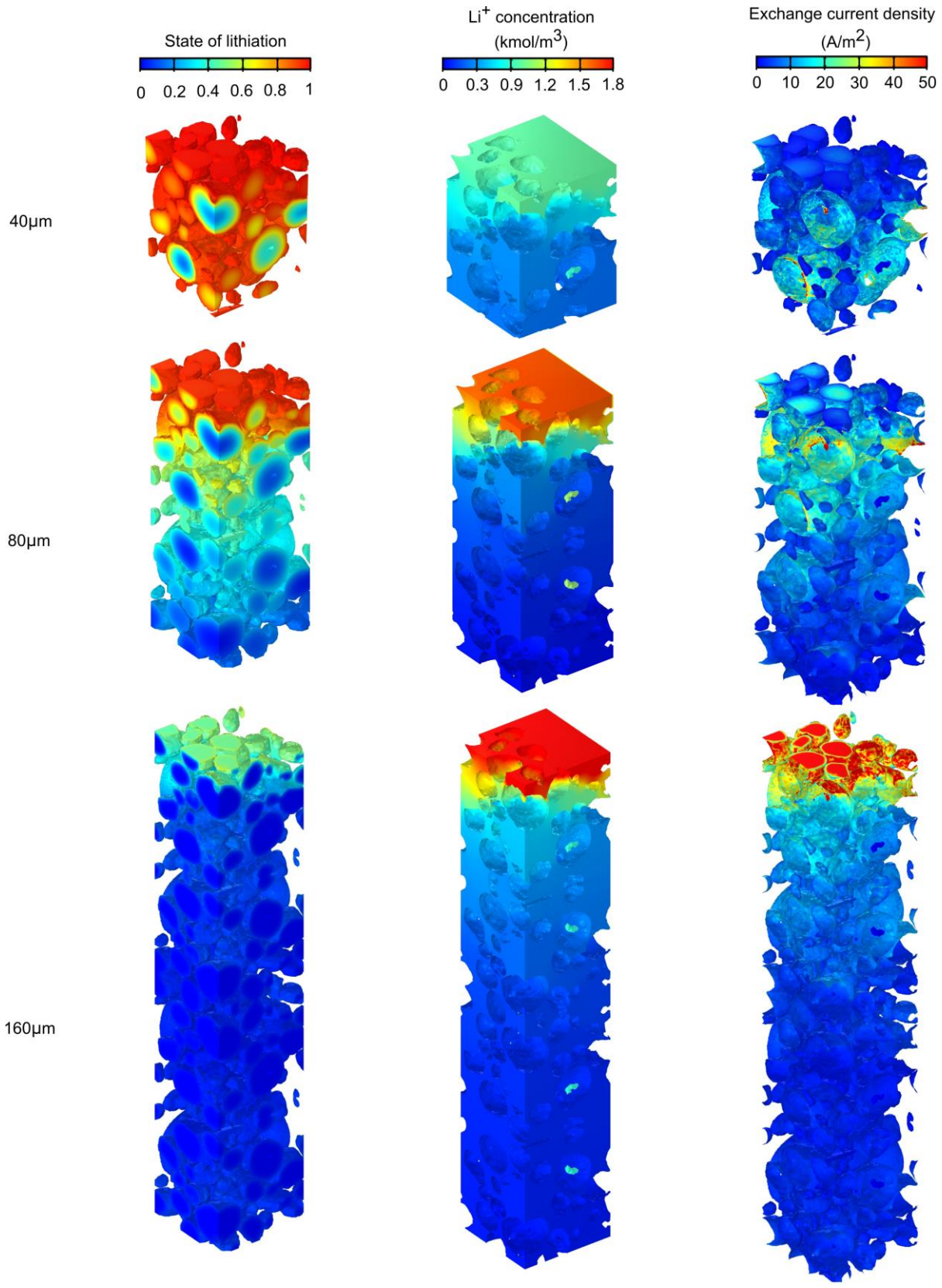

Fig. 3. State of lithiation, Li^+ concentration, and exchange current density profiles at 100% degree of discharge for electrodes of varying thickness with 25% macro-porosity. All electrodes were discharged at 5C.

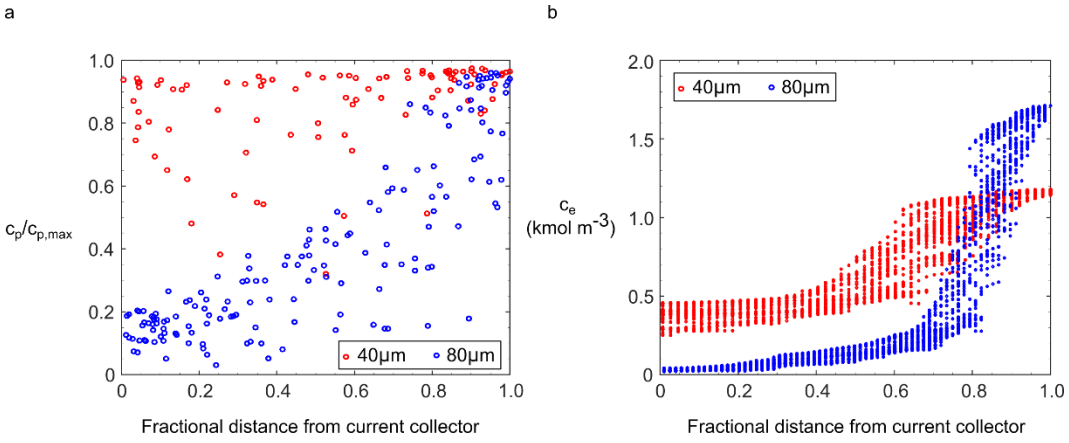

Fig. 4. (a) State of lithiation at the centre of all particles as a function of fractional distance from the current collector in the *z*-direction and (b) Li^+ concentration calculated at discrete 10 × 10 grids in the *x*-*y* plane as a function as a function of fractional distance from the current collector in the *z*-direction for 40 μm and 80 μm electrodes with 25% macro-porosity. All electrodes were discharged at 5C. Both (a) and (b) are shown at 100% degree of discharge.

3.2 Porosity-related considerations

Consider the particle lithium and electrolyte lithium-ion concentrations in Fig. 5. As with section 3.1, we also provide more detailed quantification of the state of lithiation in the centre of the particles and electrolyte concentrations at discrete 10 x 10 grid points across the thickness of the electrode in Fig. 6a and b. We show the influence of average microstructural porosity and it is clear that as macro-porosity increases the diffusion within the particles and electrolyte becomes more homogeneous, which promotes higher utilisation of active material. As porosity decreases the path becomes increasingly tortuous providing a longer effective path for species diffusion, see Tjaden et al. [43] or Lu et al. [34]. In addition, we note that increased porosity provides larger areas of exposed active particle surface, with an approximate linear relationship between the two; for example, the exposed volume specific surface area (VSSA) for 20% macro-porosity is 0.19 μm^{-1}, whilst for 40% macro-porosity the VSSA is 0.69 μm^{-1}. This facilitates more efficient use of the active materials and results in higher homogeneity in

lithium concentrations within the particles, as seen in Fig. 5 and 6a. Despite the complete lithiation of active material for a 40% macroporous electrode in Fig. 6a, there exists a corresponding small gradient in lithium-ion concentration in Fig. 6b. This can be attributed to the excess build-up of lithium-ions in the separator region of the electrode where particles have undergone full lithiation prior to the regions close to the separator; there are no reactions and thus no depletion of lithium-ions for a portion of the discharge. In addition, at 1C discharge for a thick electrode (160 μm), there remains the aforementioned sluggish diffusion behaviour that also creates such a gradient. There are downsides to increasing the porosity, such as poorer structural integrity and reduced electron transport capabilities due to the absence of CBD. The former is beyond the scope of this work whilst the latter appears to have little influence in the present study, which is a matter for future work.

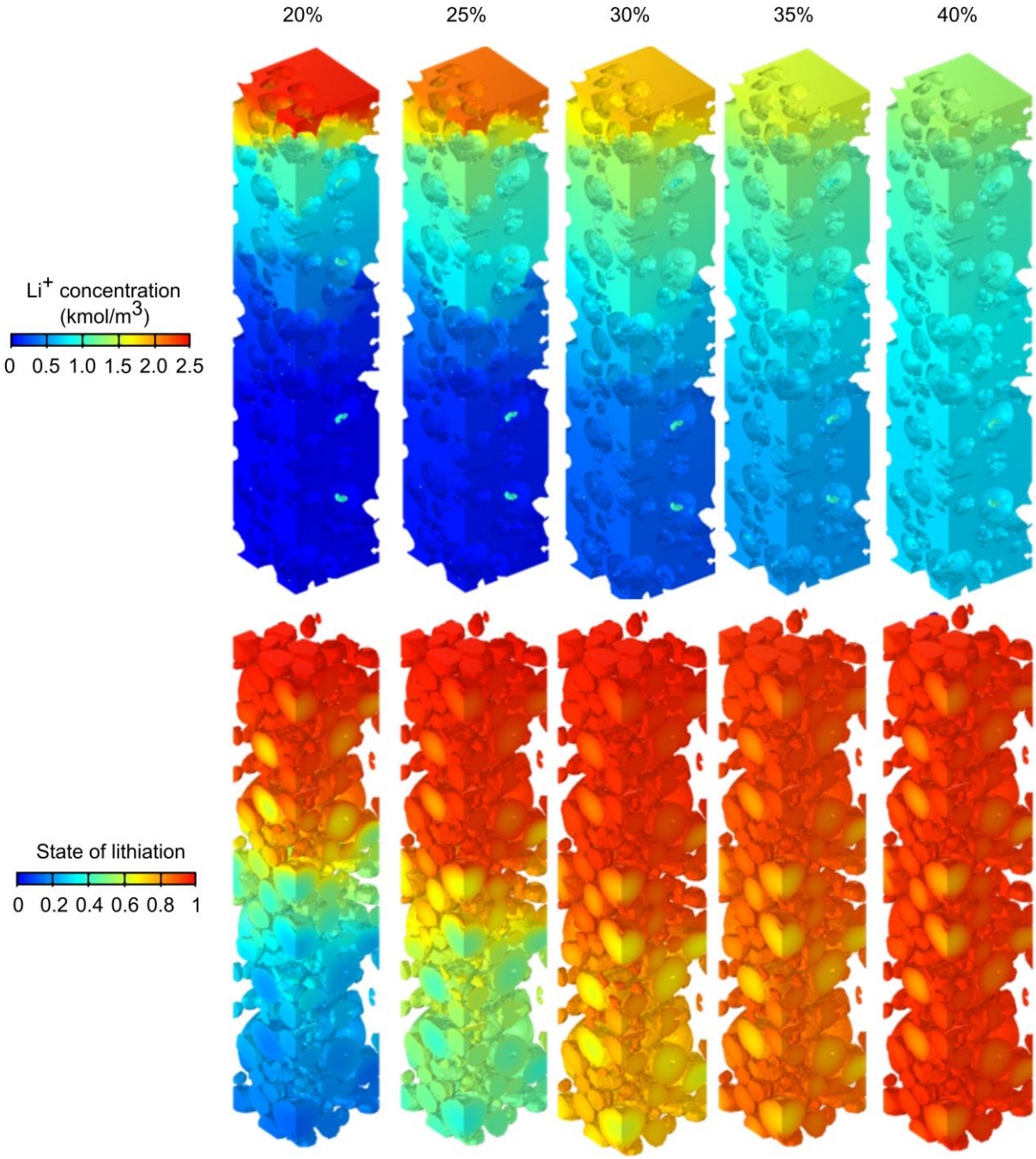

Fig. 5. State of lithiation and Li^+ concentration profiles at 100% degree of discharge for 160 µm electrodes of varying macro-porosity. All electrodes were discharged at 1C.

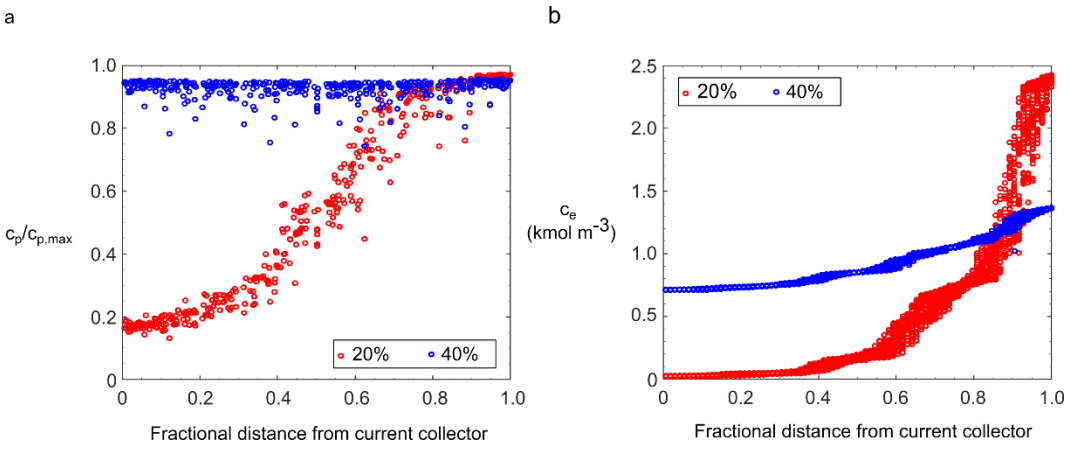

Fig. 6. (a) State of lithiation at the centre of all particles as a function of fractional distance from the current collector in the *z*-direction and (b) Li^+ concentration calculated at discrete 10 × 10 grids in the *x*-*y* plane as a function as a function of fractional distance from the current collector in the *z*-direction for 160 µm electrodes with 20% and 40% macro-porosity. All electrodes were discharged at 1C. Both (a) and (b) are shown at 100% degree of discharge.

3.3 Linking electrode porosity and thickness via discharge rate performance

Fig. 2c illustrates the impact that discharge rate has on electrode performance. It is clear that a severe reduction in electrode capacity occurs at high rate such as the 2.5C and 5C discharges. Furthermore, in Fig. 2c we observe that an upper limit on half-cell capacity exists which is dictated by discharge rate and independent of electrode thickness. These results are qualitatively in line with those of the simplified theoretical model of Heubner et al. [23]. We note that at lower macro-porosities the electrodes do not reach this upper limit, the capacity is limited by the tortuous diffusion path (which increases when the porosity is reduced) and the electrode thickness, i.e. the overall diffusion length, as described above.

If we now consider the electrode thickness, and in particular the cases of 160 µm and 320 µm thicknesses, we observe that even moderate discharge rates such as 1C result in very poor performance in terms of capacity. This exemplifies the issues associated with thick electrodes and the challenges they present in terms of real-world application in lithium-ion batteries; numerous approaches have been proposed for tailored pore architectures and functional grading to address this, and the basis for microstrucutral opimisation will be considered in the next section.

3.4 An example of thick electrodes with improved rate capabilities

Herein we present an example of rational thick electrode design through image-based modelling that addresses the previous issues and challenges as discussed. While there are myriad strategies for microsturcture engineering, we present this single, illustrative example as a demonstration of the tools outlined in this study and their utlilisation for electrode pore engineering, i.e. X-ray CT imaging combined with image proceessing and physics-based modelling.

A 160 μm electrode with 25% average macro-porosity is altered such that the half of the electrode adjacent to the separator is prescribed a 30% macro-porosity using morphological operations, while the other half on the current collector side is altered to give 20% macro-porosity; an average of 25% macro-porosity is thus maintained across the electrode. This strategy promotes improved diffusion of lithium ions further into the depths of the electrode. Such a design, when compared to the original electrode, shows improvement in discharge capacity at both 1C (7.5% increase) and 5C discharge (54% increase), see Fig 7a. The graded electrode attains greater material utilisation as seen in Fig 7b; this is achieved due to improved diffusion through the microstructure via higher levels of porosity at the separator interface adjacent to the bulk electrolyte. This example demonstrates that morphological operations and image-based simulations can be used to explore a design space for improving the energy storage and rate capabilities of thick electrodes, a matter for further work. In practice such gradations might be achieved by multi-pass printing or spray deposition approaches [44,45].

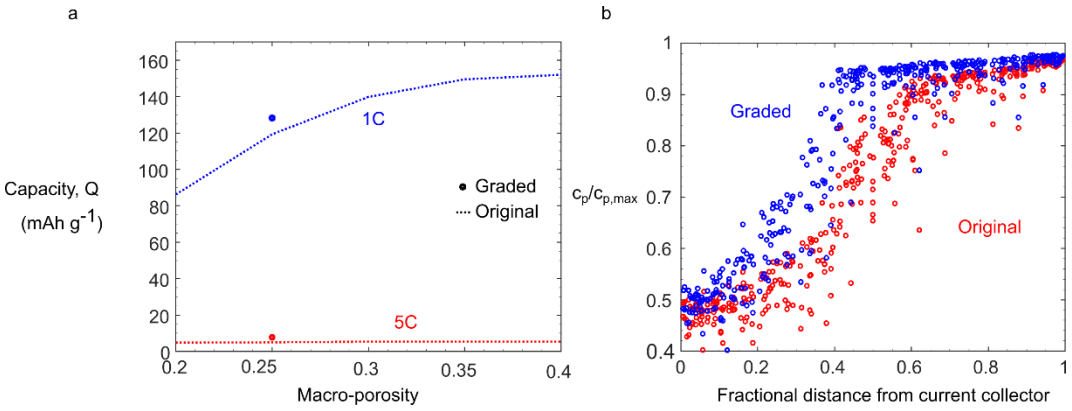

Fig. 7. (a) Comparison of the specific capacity of a graded electrode with 25% average macro-porosity versus the original simulations as shown in Fig. 2c for a 160 µm electrode discharged at 1C and 5C (b) State of lithiation at the centre of all particles as a function of fractional distance from the current collector in the *z*-direction for the original and graded electrodes with 160µm thickness and 25% macro-porosity at 100% degree of discharge. The electrode was discharged at 1C.

Conclusion

This study has provided new insight into the relationship between electrode thickness and porosity for lithium-ion batteries whilst also considering the impact of rate of discharge. We observe that the three parameters hold significant influence over the final capacity of the electrode. In particular we have seen that thick electrodes are severely limited by electrode microstructure due to species transport. An image-based approach to electrochemical modelling has highlighted the capability of capturing the significant heterogeneity that occurs within an electrode, which represents a step beyond the traditional homogenised models. Given the demonstrated ability to alter electrode microstructure via morphological operations and artificial mirroring, it is clear that image-based modelling exists as a tool to develop insight into electrode behaviour whilst also enabling design of improved realistic microstructures. A design tool which will find great use during design of thick electrodes. Further expansion of this work might consider realistic testing protocols such as pulsing and cycling. Experimental validation of the state of lithiation and electrolyte concentration profiles, in addition to the cycling response, will facilitate further understanding of the electrode microstructural design space.

Acknowledgements

This work was carried out with funding from the Faraday Institution (faraday.ac.uk; EP/S003053/1), grant number FIRG015 and FIRG025; and the EPSRC grant EP/M014045/1. The authors would like to acknowledge the Royal Academy of Engineering (CiET1718\59) for financial support.

CRediT author contribution statement

Adam M. Boyce: Conceptualization, Methodology, Software, Investigation, Data Curation, Formal analysis, Writing-Original Draft**. Xuekun Lu:** Methodology, Investigation, Writing - Review & Editing **Dan J. L. Brett:** Supervision, Project administration, Funding acquisition, Writing - Review & Editing. **Paul R. Shearing:** Conceptualization, Supervision, Project administration, Funding acquisition, Writing - Review & Editing.

Declaration of competing interest

The authors declare no competing financial interests.

References

[1] Y. Kuang, C. Chen, D. Kirsch, L. Hu, Thick Electrode Batteries: Principles, Opportunities, and Challenges, Adv. Energy Mater. 9 (2019) 1–19. https://doi.org/10.1002/aenm.201901457.

[2] A.M. Boyce, D.J. Cumming, C. Huang, S.P. Zankowski, P.S. Grant, D.J.L. Brett, P.R. Shearing, Design of Scalable, Next-Generation Thick Electrodes: Opportunities and Challenges, ACS Nano. (2021). https://doi.org/10.1021/acsnano.1c09687.

[3] M. Xu, X. Wang, Electrode Thickness Correlated Parameters Estimation for a Li-Ion

NMC Battery Electrochemical Model, ECS Trans. 77 (2017) 491–507. https://doi.org/10.1149/07711.0491ecst.

[4] H. Zheng, J. Li, X. Song, G. Liu, V.S. Battaglia, A comprehensive understanding of electrode thickness effects on the electrochemical performances of Li-ion battery cathodes, Electrochim. Acta. 71 (2012) 258–265. https://doi.org/10.1016/j.electacta.2012.03.161.

[5] M. Ebner, D.W. Chung, R.E. García, V. Wood, Tortuosity anisotropy in lithium-ion battery electrodes, Adv. Energy Mater. 4 (2014) 1–6. https://doi.org/10.1002/aenm.201301278.

[6] H. Li, L. Peng, D. Wu, J. Wu, Y.J. Zhu, X. Hu, Ultrahigh-Capacity and Fire-Resistant LiFePO 4 -Based Composite Cathodes for Advanced Lithium-Ion Batteries, Adv. Energy Mater. 9 (2019) 1–11. https://doi.org/10.1002/aenm.201802930.

[7] J.T. Lee, C. Jo, M. De Volder, Bicontinuous phase separation of lithium-ion battery electrodes for ultrahigh areal loading, Proc. Natl. Acad. Sci. U.S.A. 117 (2020) 21155–21161. https://doi.org/10.1073/pnas.2007250117.

[8] T. Wu, Z. Zhao, J. Zhang, C. Zhang, Y. Guo, Y. Cao, S. Pan, Y. Liu, P. Liu, Y. Ge, W. Liu, L. Dong, H. Lu, Thick electrode with thickness-independent capacity enabled by assembled two-dimensional porous nanosheets, Energy Storage Mater. 36 (2021) 265–271. https://doi.org/10.1016/j.ensm.2020.12.034.

[9] H. Mao, P. Shen, G. Yang, L. Zhao, X. Qiu, H. Wang, Q. Jiang, 3D highly oriented metal foam: a competitive self-supporting anode for high-performance lithium-ion batteries, J. Mater. Sci. 55 (2020) 11462–11476. https://doi.org/10.1007/s10853-020-04702-7.

[10] Y.C. Chen, Y.K. Hsu, Ultrafast Carrier Transport through an Advanced Thick Electrode with a High Areal Capacity for Aqueous Lithium-Ion Batteries, ChemSusChem. 13 (2020) 3479–3487. https://doi.org/10.1002/cssc.202000622.

[11] D. Dang, Y. Wang, S. Gao, Y.T. Cheng, Freeze-dried low-tortuous graphite electrodes with enhanced capacity utilization and rate capability, Carbon. 159 (2020) 133–139. https://doi.org/10.1016/j.carbon.2019.12.036.

[12] C. Huang, M. Dontigny, K. Zaghib, P.S. Grant, Low-tortuosity and graded lithium ion battery cathodes by ice templating, J. Mater. Chem. A. (2019) 21421–21431. https://doi.org/10.1039/c9ta07269a.

[13] R. Elango, A. Demortière, V. De Andrade, M. Morcrette, V. Seznec, Thick Binder-Free Electrodes for Li–Ion Battery Fabricated Using Templating Approach and Spark Plasma Sintering Reveals High Areal Capacity, Adv. Energy Mater. 8 (2018) 1–8. https://doi.org/10.1002/aenm.201703031.

[14] C. Huang, P.S. Grant, Coral-like directional porosity lithium ion battery cathodes by ice templating, J. Mater. Chem. A. 6 (2018) 14689–14699. https://doi.org/10.1039/c8ta05049j.

[15] J. Billaud, F. Bouville, T. Magrini, C. Villevieille, A.R. Studart, Magnetically aligned graphite electrodes for high-rate performance Li-ion batteries, Nat. Energy. 1 (2016). https://doi.org/10.1038/nenergy.2016.97.

[16] J.S. Sander, R.M. Erb, L. Li, A. Gurijala, Y.M. Chiang, High-performance battery electrodes via magnetic templating, Nat. Energy. 1 (2016) 1–7. https://doi.org/10.1038/nenergy.2016.99.

[17] M. Doyle, T.F. Fuller, J. Newman, Modeling of Galvanostatic Charge and Discharge

of the Lithium/Polymer/Insertion Cell, J. Electrochem. Soc. 140 (1993) 1526–1533. https://doi.org/10.1149/1.2221597.

[18] A.A. Franco, A. Rucci, D. Brandell, C. Frayret, M. Gaberscek, P. Jankowski, P. Johansson, Boosting Rechargeable Batteries R&D by Multiscale Modeling: Myth or Reality?, Chem. Rev. 119 (2019) 4569–4627. https://doi.org/10.1021/acs.chemrev.8b00239.

[19] H. Xu, J. Zhu, D.P. Finegan, H. Zhao, X. Lu, W. Li, N. Hoffman, A. Bertei, P. Shearing, M.Z. Bazant, Guiding the Design of Heterogeneous Electrode Microstructures for Li-Ion Batteries: Microscopic Imaging, Predictive Modeling, and Machine Learning, Adv. Energy Mater. 2003908 (2021) 1–34. https://doi.org/10.1002/aenm.202003908.

[20] S. Park, R. Tian, J. Coelho, V. Nicolosi, J.N. Coleman, Quantifying the Trade-Off between Absolute Capacity and Rate Performance in Battery Electrodes, Adv. Energy Mater. 1901359 (2019) 1–10. https://doi.org/10.1002/aenm.201901359.

[21] B. Suthar, P.W.C. Northrop, D. Rife, V.R. Subramanian, Effect of Porosity, Thickness and Tortuosity on Capacity Fade of Anode, J. Electrochem. Soc. 162 (2015) A1708–A1717. https://doi.org/10.1149/2.0061509jes.

[22] M. Xu, B. Reichman, X. Wang, Modeling the effect of electrode thickness on the performance of lithium-ion batteries with experimental validation, Energy. 186 (2019) 115864. https://doi.org/10.1016/j.energy.2019.115864.

[23] C. Heubner, M. Schneider, A. Michaelis, Diffusion-Limited C-Rate: A Fundamental Principle Quantifying the Intrinsic Limits of Li-Ion Batteries, Adv. Energy Mater. 10 (2020). https://doi.org/10.1002/aenm.201902523.

[24] B.L. Trembacki, D.R. Noble, V.E. Brunini, M.E. Ferraro, S.A. Roberts, Mesoscale Effective Property Simulations Incorporating Conductive Binder, J. Electrochem. Soc. 164 (2017) E3613–E3626. https://doi.org/10.1149/2.0601711jes.

[25] B.L. Trembacki, A.N. Mistry, D.R. Noble, M.E. Ferraro, P.P. Mukherjee, S.A. Roberts, Editors' Choice—Mesoscale Analysis of Conductive Binder Domain Morphology in Lithium-Ion Battery Electrodes, J. Electrochem. Soc. 165 (2018) E725–E736. https://doi.org/10.1149/2.0981813jes.

[26] A.N. Mistry, K. Smith, P.P. Mukherjee, Secondary-Phase Stochastics in Lithium-Ion Battery Electrodes, ACS Appl. Mater. Interfaces. 10 (2018) 6317–6326. https://doi.org/10.1021/acsami.7b17771.

[27] L.S. Kremer, A. Hoffmann, T. Danner, S. Hein, B. Prifling, D. Westhoff, C. Dreer, A. Latz, V. Schmidt, M. Wohlfahrt-Mehrens, Manufacturing Process for Improved Ultra-Thick Cathodes in High-Energy Lithium-Ion Batteries, Energy Technol. 8 (2020) 1–14. https://doi.org/10.1002/ente.201900167.

[28] S. Hein, J. Feinauer, D. Westhoff, I. Manke, V. Schmidt, A. Latz, Stochastic microstructure modeling and electrochemical simulation of lithium-ion cell anodes in 3D, J. Power Sources. 336 (2016) 161–171. https://doi.org/10.1016/j.jpowsour.2016.10.057.

[29] T. Danner, M. Singh, S. Hein, J. Kaiser, H. Hahn, A. Latz, Thick electrodes for Li-ion batteries: A model based analysis, J. Power Sources. 334 (2016) 191–201. https://doi.org/10.1016/j.jpowsour.2016.09.143.

[30] A. Quinn, H. Moutinho, F. Usseglio-Viretta, A. Verma, K. Smith, M. Keyser, D.P. Finegan, Electron Backscatter Diffraction for Investigating Lithium-Ion Electrode Particle Architectures, Cell Reports Phys. Sci. 1 (2020) 100137.

https://doi.org/10.1016/j.xcrp.2020.100137.

[31] A.C. Ngandjong, T. Lombardo, E.N. Primo, M. Chouchane, A. Shodiev, O. Arcelus, A.A. Franco, Investigating electrode calendering and its impact on electrochemical performance by means of a new discrete element method model: Towards a digital twin of Li-Ion battery manufacturing, J. Power Sources. 485 (2021) 229320. https://doi.org/10.1016/j.jpowsour.2020.229320.

[32] A.M. Boyce, E. Martínez-Pañeda, A. Wade, Y.S. Zhang, J.J. Bailey, T.M.M. Heenan, D.J.L. Brett, P.R. Shearing, Cracking predictions of lithium-ion battery electrodes by X-ray computed tomography and modelling, J. Power Sources. 526 (2022) 231119. https://doi.org/10.1016/j.jpowsour.2022.231119.

[33] S. Müller, J. Eller, M. Ebner, C. Burns, J. Dahn, V. Wood, Quantifying Inhomogeneity of Lithium Ion Battery Electrodes and Its Influence on Electrochemical Performance, J. Electrochem. Soc. 165 (2018) A339–A344. https://doi.org/10.1149/2.0311802jes.

[34] X. Lu, A. Bertei, D.P. Finegan, C. Tan, S.R. Daemi, J.S. Weaving, K.B. O'Regan, T.M.M. Heenan, G. Hinds, E. Kendrick, D.J.L. Brett, P.R. Shearing, 3D microstructure design of lithium-ion battery electrodes assisted by X-ray nano-computed tomography and modelling, Nat. Commun. 11 (2020) 1–13. https://doi.org/10.1038/s41467-020-15811-x.

[35] X. Lu, S.R. Daemi, A. Bertei, M.D.R. Kok, K.B. O'Regan, L. Rasha, J. Park, G. Hinds, E. Kendrick, D.J.L. Brett, P.R. Shearing, Microstructural Evolution of Battery Electrodes During Calendering, Joule. 4 (2020) 2746–2768. https://doi.org/10.1016/j.joule.2020.10.010.

[36] M.E. Ferraro, B.L. Trembacki, V.E. Brunini, D.R. Noble, S.A. Roberts, Electrode Mesoscale as a Collection of Particles: Coupled Electrochemical and Mechanical

Analysis of NMC Cathodes, J. Electrochem. Soc. 167 (2020) 013543. https://doi.org/10.1149/1945-7111/ab632b.

[37] J.J. Bailey, T.M.M. Heenan, D.P. Finegan, X. Lu, S.R. Daemi, F. Iacoviello, N.R. Backeberg, O.O. Taiwo, D.J.L. Brett, A. Atkinson, P.R. Shearing, Laser-preparation of geometrically optimised samples for X-ray nano-CT, J. Microsc. 267 (2017) 384–396. https://doi.org/10.1111/jmi.12577.

[38] R. Schurch, S.M. Rowland, R.S. Bradley, P.J. Withers, Comparison and combination of imaging techniques for three dimensional analysis of electrical trees, IEEE Trans. Dielectr. Electr. Insul. 22 (2015) 709–719. https://doi.org/10.1109/tdei.2014.004730.

[39] S. Singh, M.K. Kalra, J. Hsieh, P.E. Licato, S. Do, H.H. Pien, M.A. Blake, Abdominal CT: Comparison of Adaptive Statistical Iterative and Filtered Back Projection Reconstruction Techniques. 257 (2010) 373–383. https://doi.org/10.1148/radiol.10092212.

[40] K.H. Hohne, W. A. Hanson, Interactive 3D Segmentation of MRI and CT Volumes using Morphological Operations, J. Comput. Assist. Tomogr. 16 (1992) 285–294. https://doi.org/10.1097/00004728-199203000-00019

[41] D. Chudasama, T. Patel, S. Joshi, G.I. Prajapati, Image Segmentation using Morphological Operations, Int. J. Comput. Appl. 117 (2015) 16–19. https://doi.org/10.5120/20654-3197

[42] C. Miehe, M. Hofacker, F. Welschinger, A phase field model for rate-independent crack propagation: Robust algorithmic implementation based on operator splits, Comput. Methods Appl. Mech. Eng. 199 (2010) 2765–2778.

https://doi.org/10.1016/j.cma.2010.04.011.

[43] B. Tjaden, S.J. Cooper, D.J. Brett, D. Kramer, P.R. Shearing, On the origin and application of the Bruggeman correlation for analysing transport phenomena in electrochemical systems, Curr. Opin. Chem. Eng. 12 (2016) 44–51. https://doi.org/10.1016/j.coche.2016.02.006.

[44] S.H. Lee, C. Huang, P.S. Grant, Multi-layered composite electrodes of high power Li4Ti5O12 and high capacity SnO2 for smart lithium ion storage, Energy Storage Mater. 38 (2021) 70–79. https://doi.org/10.1016/j.ensm.2021.02.010.

[45] C. Cheng, R. Drummond, S.R. Duncan, P.S. Grant, Combining composition graded positive and negative electrodes for higher performance Li-ion batteries, J. Power Sources. 448 (2020) 227376. https://doi.org/10.1016/j.jpowsour.2019.227376.